THE JOURNAL OF BIOLOGICAL CHEMISTRY
Vol. 279, No. 51, Issue of December 17, pp. 52860–52868, 2004

Printed in U.S.A.

Effect of Axial Coordination on the Kinetics of Assembly and Folding of the Two Halves of Horse Heart Cytochrome *c**

Received for publication, March 22, 2004, and in revised form, September 15, 2004
Published, JBC Papers in Press, Septmeber 22, 2004, DOI 10.1074/jbc.M403127200

Giampiero De Sanctis‡, Chiara Ciaccio§, Giovanni Francesco Fasciglione§, Laura Fiorucci§, Magda Gioia§, Federica Sinibaldi§, Stefano Marini§, Roberto Santucci§, and Massimo Coletta§¶

From the ‡Department of Molecular, Cellular and Animal Biology, University of Camerino, Via F. Camerini 2, I-62032 Camerino, Italy and the §Department of Experimental Medicine and Biochemical Sciences, University of Roma Tor Vergata, Via Montpellier 1, I-00133 Roma, Italy

The kinetics of the assembly of two complementary fragments of oxidized horse heart cytochrome *c* (cyt *c*), namely the heme-containing fragment-(1–56) and the fragment-(57–104), have been characterized at different pH values. At neutral pH the fragment-(1–56) is hexacoordinated and has two histidines axially ligated to the heme-Fe(III) (Santucci, R., Fiorucci, L., Sinibaldi, F., Polizio, F., Desideri, A., and Ascoli, F. (2000) *Arch. Biochem. Biophys.* 379, 331–336), thus mimicking what occurs in the folding intermediate of cyt *c*. The kinetics of the formation of the complex between the two fragments are characterized at pH 7.0 by a slow rate constant that is independent of the concentration of the reactants; conversely, at a low pH the kinetics are much faster and depend on the concentration of the fragments. This behavior suggests that the rate-limiting step observed in the recombination process of the fragments at neutral pH (that leads to the final coordination of Met-80) has to be ascribed to the detachment of the "misligated" histidine. Thus, the faster recombination rate at a low pH can be related to the fact that histidine is protonated and not able to coordinate to the metal. Furthermore, the independence of the rate constant on the concentration of the reactants observed at pH 7.0 can be accounted for by the occurrence of a conformational transition, which takes place immediately after the two fragments collapse together, likely simulating what induces the detachment of the misligated histidine during cytochrome folding.

Protein folding is a central topic in the modern structural biology and has attracted a great deal of interest in the last decade. Several studies have elucidated that many small proteins fold rapidly to the unique native state following a simple two-state process (1), but large proteins generally reach the biologically active conformation through a multistate way. Starting with the pioneering work of Eaton and co-workers (2), the introduction of fast kinetic methods for the detection of intermediate states has opened new scenarios in the description of the protein folding process (for a review, see Refs. 3 and 4). In this context, cytochrome *c* (cyt *c*)[1] represents an ideal system to investigate, because it is one of the most studied proteins (5) and its high-resolution x-ray structure is available (6).

The folding of cyt *c* is characterized by a variety of long lived intermediates, some of which are ascribed to proline isomerization (7), whereas others are referable to non-native heme ligation (8, 9). An important aspect in the kinetic study of cyt *c* folding is the formation at a neutral pH of a misligated compact intermediate having a histidine side chain (His-26 or His-33) axially ligated to the sixth coordinate position of the heme-Fe(III) in place of Met-80 (the residue coordinated to the metal in the native protein) (10, 11). Although it has been proposed to be an on-pathway intermediate (12), the non-native His-Fe(III) ligation indeed represents a kinetic barrier for the folding of the polypeptide into the native conformation, therefore sensibly reducing the protein folding rate (13). This is confirmed by the fact that at an acidic pH, the folding of cyt *c* proceeds faster, being that histidines are largely protonated (14).

The peptide fragments of cyt *c* can be achieved by a limited proteolysis of the protein (15). Recently, the properties of a 56-residue heme-containing fragment (here indicated as fragment 1 (F1), with the amino acid sequence corresponding to residues 1–56 of native horse cyt *c*) have been determined (16), and F1 turns out to be hexacoordinated and largely disordered. Like the native protein, F1 retains His-18 axially bound to the metal, but the other axial ligand of the heme-iron is proposed to be a histidine residue (His-26 or His-33) in place of Met-80 (a residue not present in the fragment sequence, see Fig. 1).

Recently, the complex reconstituted from F1 and its complementary fragment-(57–104) (here indicated as F2) has been achieved, and its structural and functional properties have been determined (17). At a neutral pH the fragment complex shows a native-like α-helix structure and His-18-Fe(III)-Met-80 axial coordination to the heme. This suggests that the fragment recombination to form the complex implies an axial ligand displacement from a His-Fe(III)-His to a His-Fe(III)-Met coordination.

The goal of the present kinetic investigation is a deeper understanding of the events associated with the axial ligand exchange at the sixth coordination position of the heme-Fe(III) during complex formation, a process that leads to the native His-18-Fe(III)-Met-80 coordination. Such an approach is expected to provide a relevant contribution to better clarify the mechanism(s) governing the last steps of the cyt *c* folding pathway.

* This work has been financially supported by the Italian Ministero dell'Istruzione, Università e Ricerca (MIUR COFIN 2001031798). The costs of publication of this article were defrayed in part by the payment of page charges. This article must therefore be hereby marked "*advertisement*" in accordance with 18 U.S.C. Section 1734 solely to indicate this fact.

¶ To whom correspondence should be addressed: Dept. of Experimental Medicine and Biochemical Sciences, University of Roma Tor Vergata, Via Montpellier 1, I-00133 Roma, Italy. Tel.: 39-06-72596365; Fax: 39-06-72596353; E-mail: coletta@seneca.uniroma2.it.

[1] The abbreviations used are: cyt *c*, oxidized horse heart cytochrome *c*; F1, fragment corresponding to the residues 1–56 of cytochrome *c*; F2, fragment corresponding to residues 57–104 of cytochrome *c*.

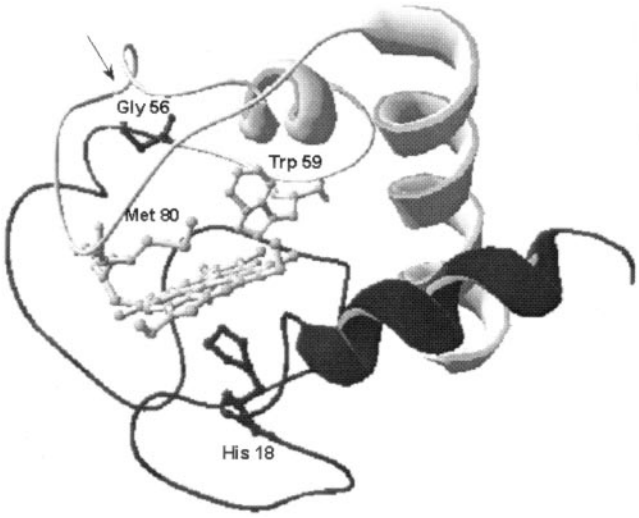

FIG. 1. **Structural representation of horse heart cytochrome *c*.** The two fragments have been drawn in different colors, namely the fragment 1–56 (F1) is drawn as a *dark rubber line*, whereas the fragment 57–104 (F2) is drawn as a *white* rubber *line*. *Arrow* shows where cleavage in two fragments occurs. For further details, see text.

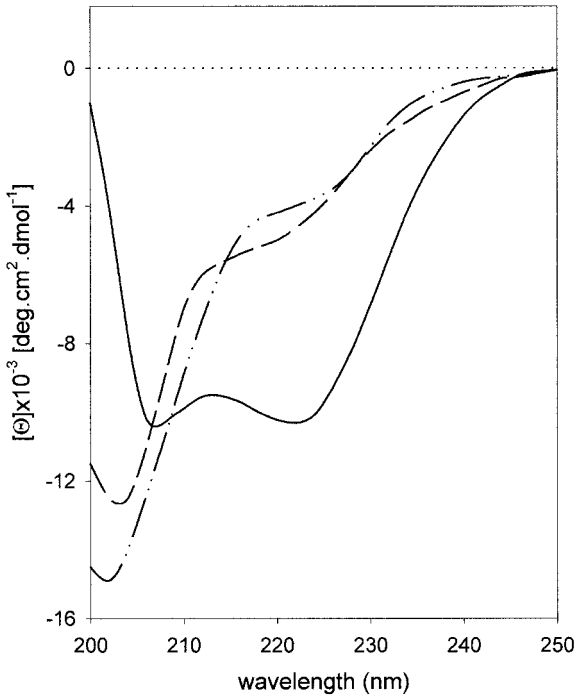

FIG. 2. **Far-UV circular dichroism spectra at pH 7.0 of the cyt *c* complex (*continuous line*) of the 1–56 F1 complex (*dashed line*) and of the 57–104 F2 complex (*dashed-dotted line*) are shown.**

EXPERIMENTAL PROCEDURES

Oxidized horse heart cyt *c* (type VI) and thermolysin were obtained from Sigma and used without further purification. All other reagents were of analytical grade.

The digestion of cyt *c* and purification of F1-(1–56) and F2-(57–104) were performed as previously described (15, 16). The fragments were used immediately after preparation and purification. Absorption spectra have been obtained using a Varian V-530 spectrophotometer, and circular dichroism spectra have been obtained using a Jasco J-700 spectrometer equipped with PC as data processor.

Kinetic studies following optical absorption changes have been carried out using a SX.18MV stopped flow (Applied Photophysics, Salisbury, UK) with a 1-ms dead time. Experiments have been undertaken mixing F1, dissolved in the desired environment (pH 7.0 or 3.8), with F2 previously dissolved at pH 7.0 and very low ionic strength. The final pH was measured directly on the final mixture, and it was considered the actual pH at which the reaction occurred. The progress curves were recorded at several different wavelengths (*e.g.* 280, 408, or 695 nm) to acquire more complete spectroscopic information on the processes taking place.

CD kinetic measurements have been carried out employing a rapid-mixing apparatus SFM-20 (Biologic Science Instruments) with 8-ms dead time and interfaced with the Jasco J-700 spectrometer. The setting of the experiment was closely similar to that employed for optical absorption kinetics (see above), but the investigation has been limited to pH 7.0. Experiments were undertaken at 20 °C.

RESULTS AND DISCUSSION

The far-UV CD spectrum of the complex has been reported previously (16, 17). In Fig. 2, the far-UV circular dichroism spectra of the two isolated fragments are compared with that of the complex recorded under the same conditions. The far-UV CD clearly indicates that the two isolated fragments possess a substantially disordered structure, characterized by negligible α-helical content (see Fig. 2). The CD spectrum is unaffected by pH down to a value of 3 (data not shown). On the other hand, the complex formation brings about a CD signal revealing the appearance of an α-helical conformation comparable with that of native cyt *c* (see Fig. 2 and Ref. 16). This process is characterized by a strong association equilibrium constant, because essentially 100% of the complex formation is observed already at $\cong$0.1 μM concentration (*i.e.* a value ~20-fold lower than what was employed throughout this study).

The pH dependence of the Soret absorption spectra of F1 and of the fragment complex are shown in Fig. 3, *A* and *B*, respectively. Fig. 3*C* displays the pH dependence of the circular dichroism of the complex over the same wavelength range. At pH 7.0 the absorption spectrum of F1 is virtually identical to that of the complex (see Fig. 3, *A* and *B*), with both showing a maximum at 406 nm. Unlike absorption, the dichroic spectrum of F1 at pH 7.0 differs significantly from that of the fragment complex; in particular, it misses the negative 416-nm Cotton effect (see Ref. 16). This is not surprising, because in the native cyt *c* the 416-nm signal is ascribed to the Met-80-Fe(III) axial coordination (18). In the Soret CD spectrum of the fragment complex at pH 7.0 (see Fig. 3*C*) this signal is observed, being consistent with the Met-80-Fe(III) coordination. Some minor heterogeneity is observed in solution, as revealed by the blue shifts of the Cotton effects (414 *versus* 416 nm and 401 *versus* 406 nm) and by the lower intensity of the 416-nm Cotton effect of the fragment complex with respect to the native cyt *c* (5).

As the pH is lowered, the absorption band is blue-shifted from 406 to 396 nm (for F1 alone) and to 395 nm (for the complex) (see Fig. 3, *A* and *B*), while the CD spectrum of the complex displays the progressive disappearance of the negative 416-nm Cotton effect, associated with the progressive enhancement of the 402-nm Cotton effect (which is also blue-shifted to 398 nm, see Fig. 3*C*). The pH dependence of absorption spectra, followed at 406 nm, clearly indicates the occurrence of a transition from the hexa- to the pentacoordination of the heme, which is characterized by a pK_a = 4.21 ($\pm$0.16) for F1 and by pK_a = 3.18 ($\pm$0.18) for the complex (see Fig. 4*A*). Thus, in F1 pentacoordination takes place at a higher pH with respect to the complex, indicating that detachment of the axially "misligated" histidine from the metal in the fragment F1 requires less energy than detachment of Met-80 in the fragment complex. This interpretation indeed seems supported by the features observed in the pH-dependent behavior of the CD spectra, where the pH-induced transition in the fragment complex (followed through the progressive disappearance of the 416-nm Cotton effect, see Fig. 3*C*) shows a similar pK_a value (3.23 $\pm$ 0.17, see Fig. 4*B*).

Therefore, as previously reported (17), mixing F1 with F2 at a neutral pH brings about the formation of a complex charac-

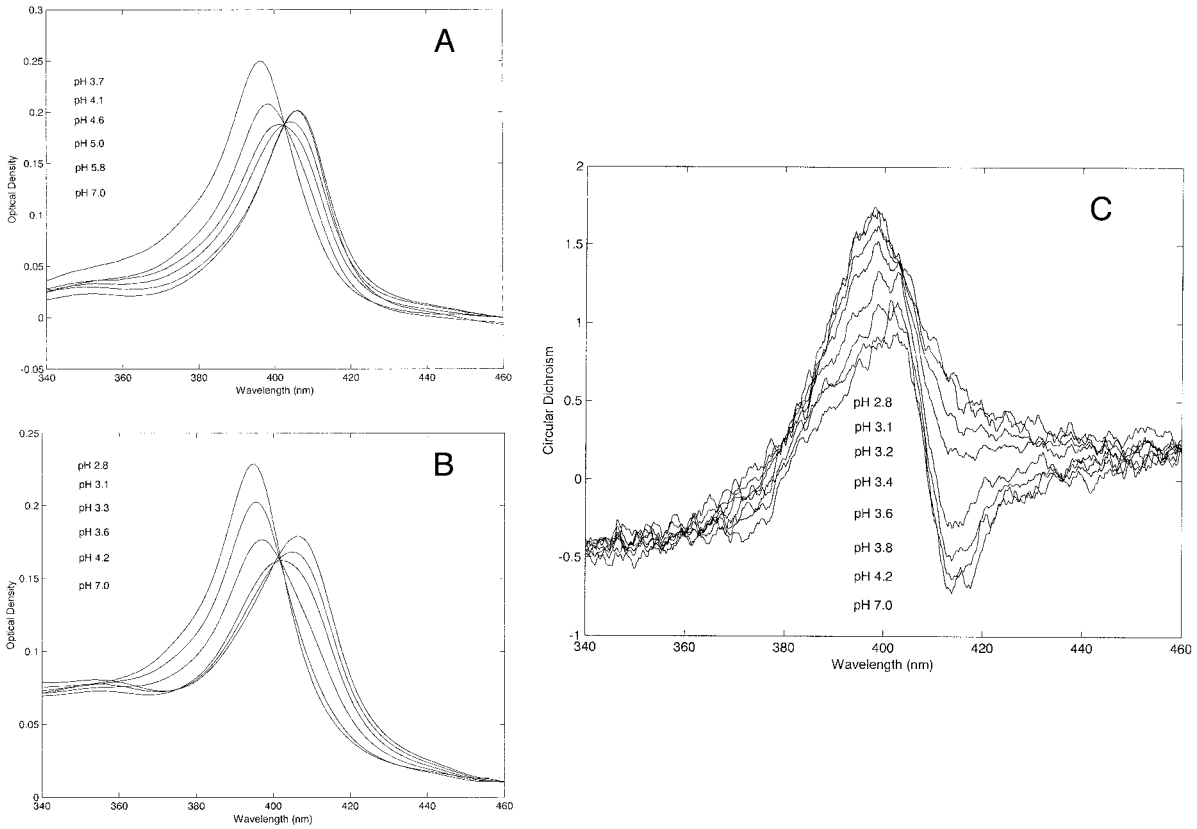

FIG. 3. **pH dependence of absorption spectra of F1 fragment (*A*), the F1 + F2 complex (*B*) and of the circular dichroism spectra of the complex (*C*).** pH values reported in the three panels correspond to those at which the spectra have been collected, following the direction of spectra closer to the digits. For further details, see text.

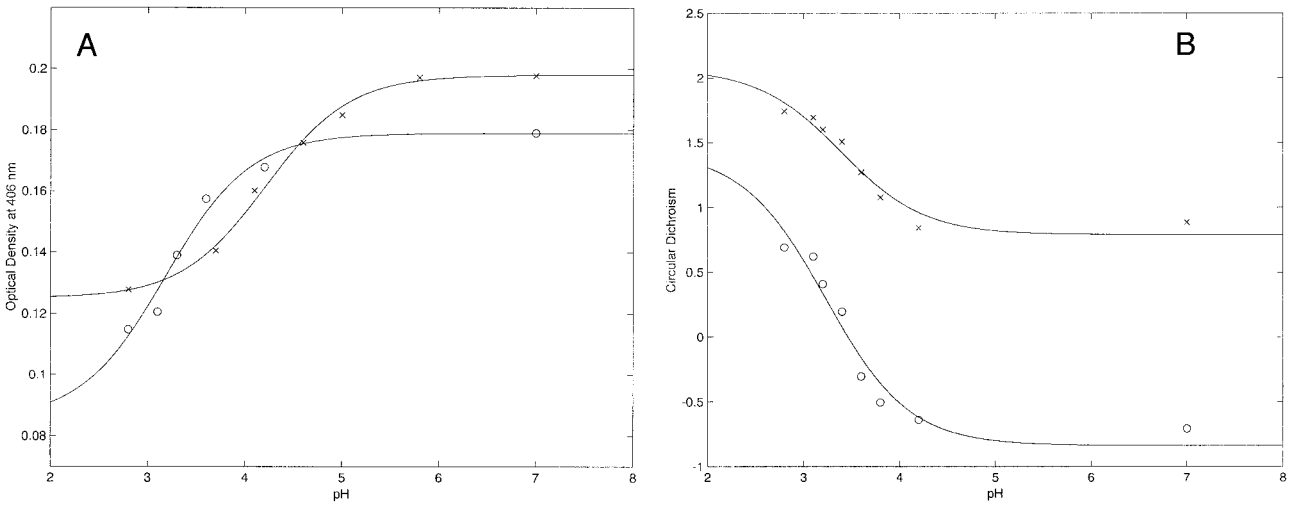

FIG. 4. **pH dependence of the absorption at 406 nm for the F1 fragment (*x*) and for the complex (*o*) (*A*), and pH dependence of the circular dichroism at 414 nm (*o*) and at 398 nm (*x*) (*B*) are shown.** In both panels, *continuous lines* are the non-linear least-squares fitting of data, employing the equation $P_{obs} = P_0 + \Delta P \cdot K_a \cdot [H^+]/(1 + K_a \cdot [H^+])$, where P_{obs} is the observed value of the parameter (either OD or CD) at a given pH value, P_0 is the value of the parameter extrapolated to infinitely low $[H^+]$, ΔP is the total pH-dependent variation of the parameter (which can have either a positive or a negative value), K_a is the proton affinity constant (defined as $K_a = 10^{pKa}$). Continuous lines have been obtained with following parameters. *A*, for F1, $P_0 = 0.198 \pm 0.021$, $\Delta P = -0.073 \pm 0.008$, $pK_a = 4.21 \pm 0.16$; for the complex, $P_0 = 0.179 \pm 0.019$, $\Delta P = -0.094 \pm 0.011$, $pK_a = 3.18 \pm 0.18$. *B*, for the complex at 414 nm, $P_0 = -0.837 \pm 0.094$, $\Delta P = 2.27 \pm 0.24$, $pK_a = 3.23 \pm 0.17$; for the complex at 398 nm, $P_0 = 0.791 \pm 0.083$, $\Delta P = 1.28 \pm 0.15$, $pK_a = 3.39 \pm 0.18$. For further details, see text.

terized by a compact close-to-native tertiary assembly, in which a His is replaced by Met-80 from the axial coordination to the heme-Fe (III). On the other hand, the different pK_a values for the pH-dependent transition of F1 and of the complex (see Fig. 4) indeed suggest that at pH 3.8 the formation of the complex can be achieved in the absence of a misligated His (19). The kinetics of complex formation as a function of F1 concentration was followed at the two pH values and at three distinct wavelengths, namely at 695 nm (to directly follow the formation of the Fe(III)-Met-80 bond, see Ref. 20), at 408 nm (to follow the evolution of the axial coordination at the heme), and at 280 nm (exploiting the change of Trp-59 absorption to follow directly the complex formation, see Ref. 17).

Fig. 5*A* shows the kinetics of the Fe(III)-Met-80 bond forma-

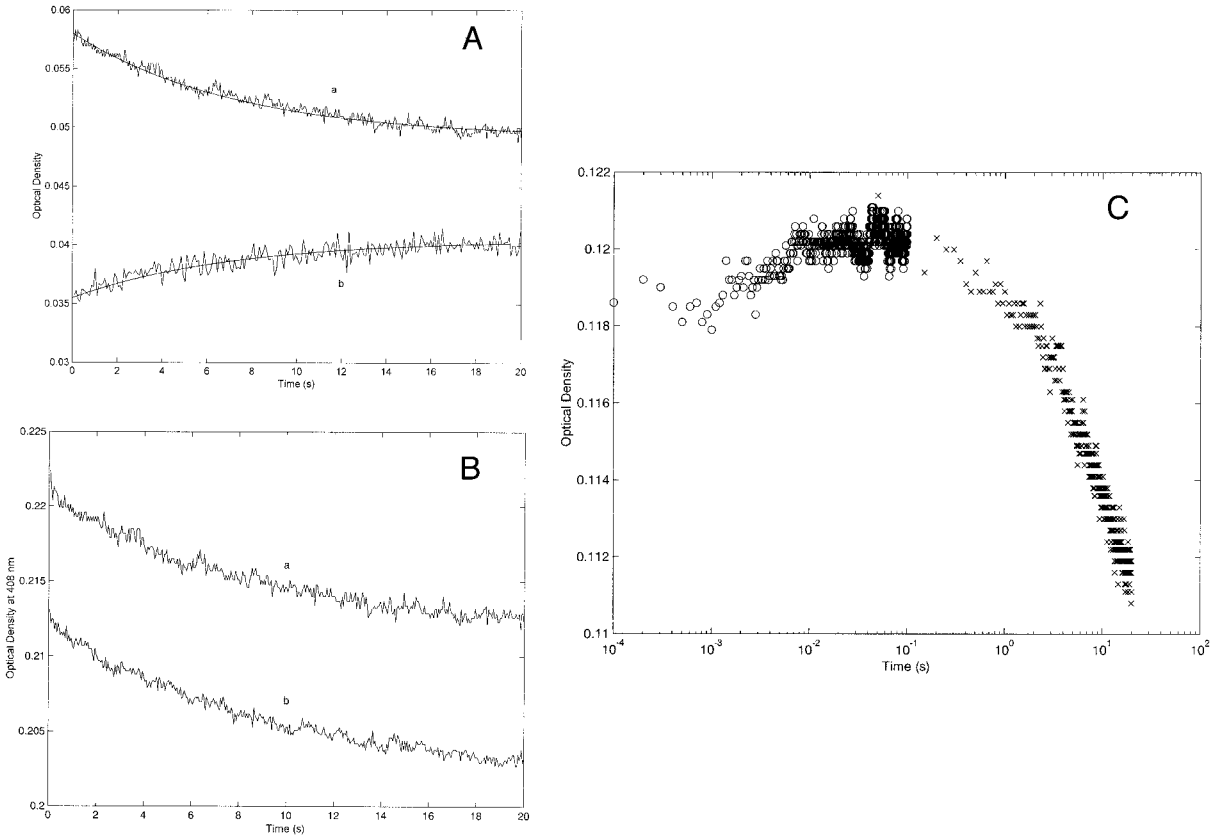

FIG. 5. **Kinetic progress curves of complex formation.** *A*, progress curves at 408 nm (*curve a*) and at 695 nm (*curve b*) following the mixing of 12.5 μM F1 with 2.5 μM F2. The absolute optical density of the two progress curves (but not the optical density change) has been scaled to make them fit into a limited range of optical density. Least-squares fitting of progress curves has been carried out according to the following analytical equation $S_{obs} = S_\infty + \Delta S \cdot e^{(-k \cdot t)}$, where S_{obs} is the observed signal (either optical density or circular dichroism), S_∞ is the final signal (either optical density or circular dichroism), ΔS is the variation of signal (either optical density or circular dichroism), which can have either a positive or negative value (according to whether the observed signal decreases or increases as a function of time), k is the (pseudo)first-order rate constant and t is time. Continuous curves correspond to least-squares fitting of progress curves according to this equation, employing the following parameters: *curve a*, $S_\infty = 0.049 \pm 0.005$, $\Delta S = 0.009 \pm 0.001$, $k = 0.143 \pm 0.016$; *curve b*, $S_\infty = 0.040 \pm 0.005$, $\Delta S = -0.005 \pm 0.001$, $k = 0.148 \pm 0.017$. *B*, progress curves at 408 nm following the mixing of 2.5 μM F2 with 12.5 μM F1 (*curve a*) or with 3.1 μM F1 (*curve b*). The optical density of the two progress curves has been scaled (keeping intact the change in optical density), to make them fit into a limited range of optical density and to immediately compare them. *C*, kinetic progress curves of the complex formation at pH 7.0 following the mixing of 12.5 μM F1 with 2.5 μM F2 at 280 nm (*o*) and at 408 nm (*x*). The two progress curves have been reported on a logarithmic time scale, and their optical density has been scaled to have overlapping values of optical density for experimental points at the same time interval. For further details, see text.

tion at pH 7.0, following the absorption change at 695 nm; a closely similar progress curve is obtained at 408 nm, clearly indicating that we are observing the same event at the two wavelengths. However, the much higher extinction efficient at 408 nm renders this last wavelength more preferable for working at a low protein concentration.

A very peculiar aspect of the kinetics observed at pH 7.0, associated with the events occurring at the heme pocket (*i.e.* at 408 and 695 nm), is that both the rate constant of the complex formation and the corresponding amplitude of the absorption change turned out to be independent from the concentration of F1 with an apparent rate constant of 0.14 ($\pm$0.03) s^{-1} (see Fig. 5*B*). Conversely, the rate observed at 280 nm is linearly dependent on the concentration of F1, as expected for a bimolecular process (Fig. 6), giving a second-order association rate constant of 7.2 ($\pm$0.8) $\times$ 10^6 M^{-1} s^{-1} at pH 7.0 and a dissociation rate constant of 22.0 ($\pm$2.5) s^{-1}. Therefore, the analysis of data at different wavelengths provides two kinds of information, namely the complex formation rate constant, which is fast (from observations at 280 nm, see Fig. 5*C*) and the rate of replacement of the misligated His by Met-80, which occurs only at a later stage (as monitored at 408 and 695 nm, see Fig. 5, *A* and *C*).

On the basis of the results obtained at pH 7.0, we are thus expecting at lower pH values a much faster rate at 408 nm (similar to that at 280 nm), because most of F1 does not undergo His misligation (see Figs. 3 and 4). Indeed, at pH 3.8 we observe a much faster progress curve (see Fig. 7), and the rate of the optical change at 408 nm now depends on the concentration of F1, like at 280 nm (see Fig. 6), displaying a second-order rate constant at pH 3.8 (5.6 ($\pm$0.6) $\times$ 10^6 M^{-1} s^{-1}), which is similar, although not identical, to that obtained for the fragment complex formation at pH 7.0 (followed at 280 nm, see Fig. 6). Therefore, this result shows that the complex formation occurs at a rate that is essentially pH-independent from the pH range between 3.8 and 7.0, suggesting that the recognition process between the two fragments in not modulated by residues that protonate within this pH range. On the other hand, the dissociation rate constant of the complex at pH 3.8 (3.5 s^{-1}) is much slower than at pH 7.0, indicating a higher stability of the assembled form at lower pH possibly because of the protonation of some residue. This suggests that ionic interactions are important for the stability of the complex between the two fragments. It also strengthens the idea that pH lowering does not alter drastically the association equilibrium constant; the overall value of the constant is related not only to the complex formation of the two fragments collapsing together but also to the thermodynamics of different steps leading to the final native-like His-18-Fe(III)-Met-80 form.

At this point, we can give a first sketch of the various steps

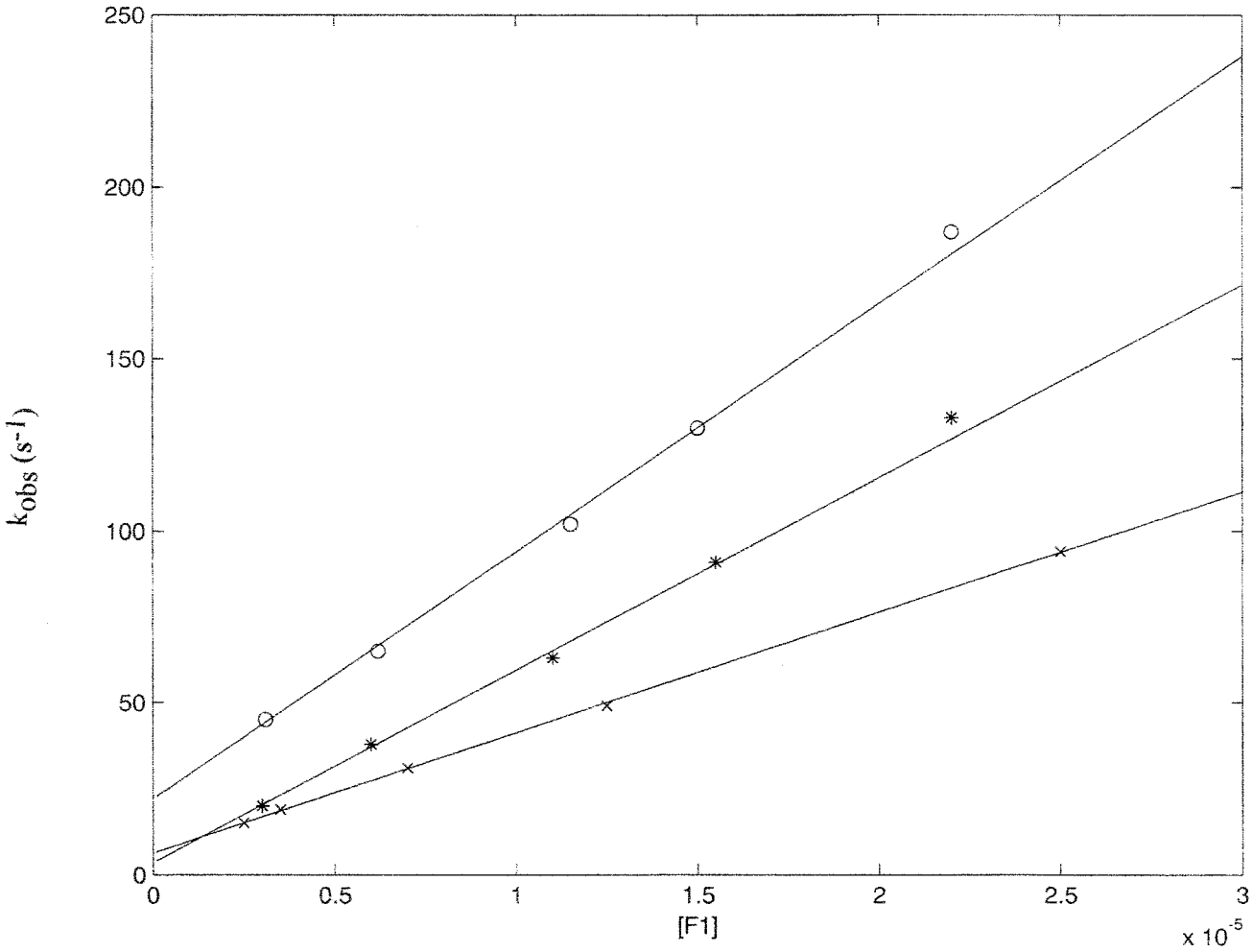

FIG. 6. **Dependence of the observed rate constant for the mixing of F1 with F2 (k_{obs}, s^{-1}) on the concentration of F1.** The observed rate constants have been collected at pH 7.0 at 280 nm (*o*), at pH 3.8 at 408 nm (*x*) and at 280 nm (*). The *continuous lines* correspond to the non-linear least-squares fitting of data according to the equation $k_{obs} = k_{on}\cdot[F1] + k_{off}$, where k_{obs} is the observed rate constant at a given concentration of F1, k_{on} is the second-order association rate constant for the complex formation and k_{off} is the dissociation rate constant of the complex. *Continuous lines* have been obtained with following parameters: pH 7.0 at 280 nm, $k_{on} = 7.2\ (\pm 0.8) \times 10^6\ M^{-1}\ s^{-1}$, $k_{off} = 22.0\ (\pm 2.5)\ s^{-1}$; for pH 3.8 at 408 nm, $k_{on} = 3.5\ (\pm 0.4) \times 10^6\ M^{-1}\ s^{-1}$, $k_{off} = 6.3\ (\pm 0.7)\ s^{-1}$; for pH 3.8 at 280 nm, $k_{on} = 5.6\ (\pm 0.6) \times 10^6\ M^{-1}\ s^{-1}$, $k_{off} = 3.5\ (\pm 0.4)\ s^{-1}$. For further details, see text.

characterizing the complex formation at neutral pH. In the first step of Scheme 1, the collapse of the two fragments brings about the formation of an initial complex (called Complex 1), in which no change in the heme coordination occurs (corresponding to the process followed at 280 nm). In the following step, the dissociation of the misligated His takes place, giving rise to a pentacoordinated species (called Complex 2). Finally, Met-80 coordinates to the metal, and the final native-like Met-80-Fe(III) coordinated form (indicated as Complex 3) is stabilized. The different observations obtained at 280 nm with respect to those collected at 408 and 695 nm may indeed be related to the fact that at 280 nm we are following the formation of Complex 1, whereas at 408 and 695 nm we are detecting the formation of Complex 3 (see Fig. 5*C*). From the application of Scheme 1 it turns out also that the rate of formation of Complex 2 (associated to the dissociation of the misligated His) is the rate-limiting step for the evolution toward the native-like Complex 3 (see also Fig. 5*C*).

However, to prove the applicability of this scheme we must be able to simulate quantitatively its behavior, taking into account the features displayed by the system. Therefore, computer simulations of the time evolution of different populations of complexes according to Scheme 1 (as well as of the following Scheme 2) have been carried out employing a Runge-Kutta second-order algorithm in which the time evolution of the individual populations was reckoned for each individual time step *x*, taking into account the rates of their formation and of their disappearance. Thus, as an example, for Complex 2 from Scheme 1, the calculation for each step was as follows,

$$[[\text{Complex 2}]_t = [\text{Complex 2}]_{t-x} + (k_{+2}\cdot[\text{Complex 1}]_{t-x} + k_{-3}\cdot[\text{Complex 3}]_{t-x} - [\text{Complex 2}]_{t-x}\cdot(k_{-2} + k_{+3}))\cdot x] \quad \text{(Eq. 1)}$$

In this respect, one important observation (reported in Fig. 5*B*) indicates that at pH 7.0 the rate of the absorption change at 408 nm (following the formation of Complex 3) remains constant, independently from the concentration of F1. It suggests that according to Scheme 1 the amount of Complex 1 transforming into Complex 2 is not dependent on the concentration of F1, at least within the F1 concentration range investigated. A computer simulation of the behavior of the system according to Scheme 1 has been carried out, employing the bimolecular rate constant for the formation of Complex 1 as calculated on the basis of data reported in Fig. 6. An arbitrary set of rate constants has been employed for the additional steps, whose values refer to the gross kinetic relationships among different steps, accounting for faster and slower processes (see Table I). However, the simulation obtained accord-

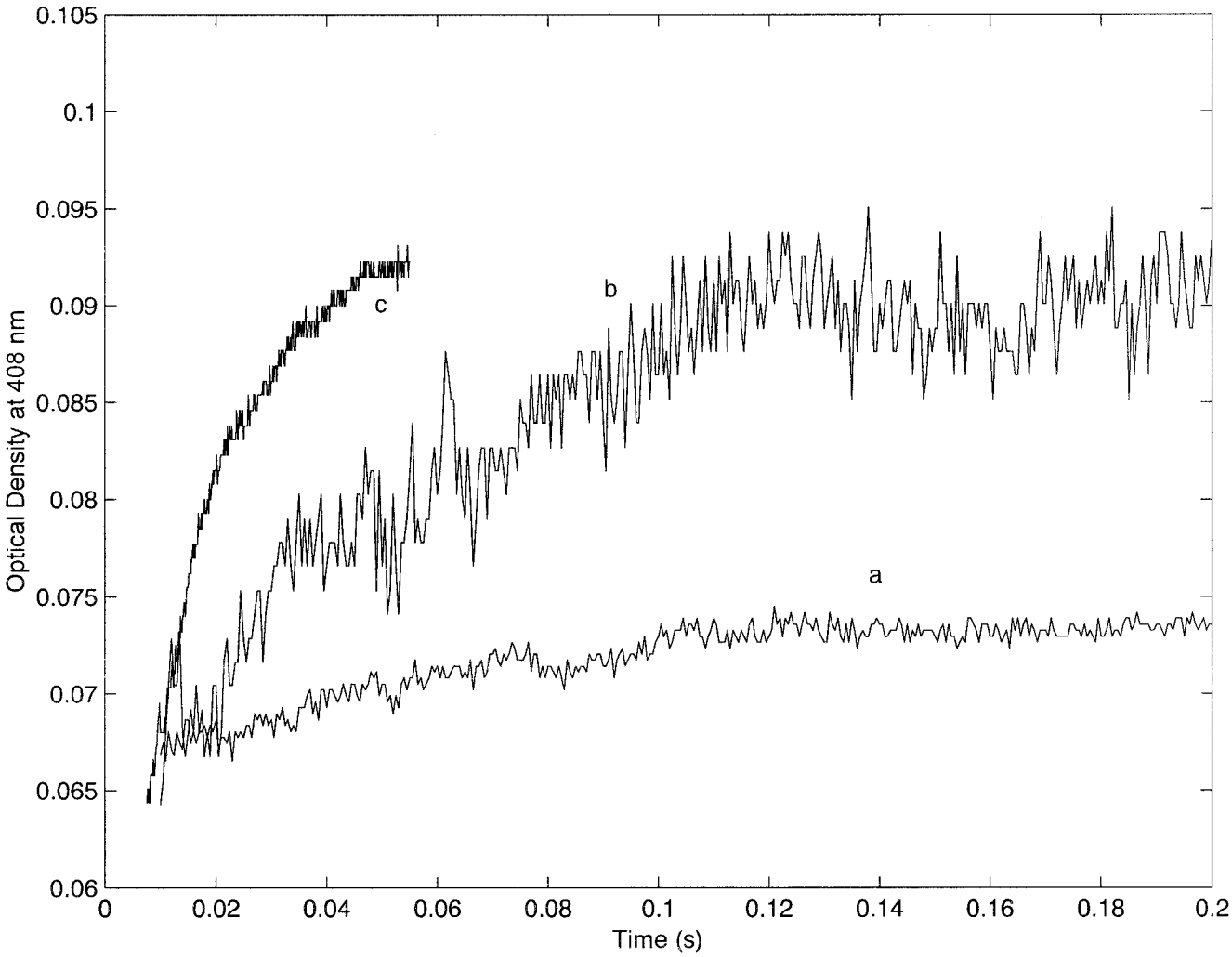

FIG. 7. **Progress curves at 408 nm, following the mixing at pH 3.8 of 2.5 μM F2 with 3.1 μM F1 (*curve a*), 6.2 μM F1 (*curve b*), and 25 μM F1 (*curve c*).** The progress curves have been scaled to have a closely similar optical density at $t \cong 0$. Because even at pH 3.8 there is still a fraction of misligated His (ranging between 10 and 15%), the actual progress curves also display a very slow fraction (not shown here), whose rate closely resembles that observed at pH 7.0 (see legend to Fig. 3) and the amplitude corresponds to the percentage fraction of misligated His. For further details, see text.

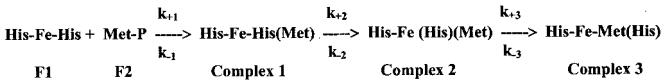

SCHEME 1

ing to Scheme 1 indicates that even keeping constant the concentration of F2 (as it occurs in our experiments), the rate of formation of Complex 3 (observed at 408 nm) is dependent on the concentration of F1 over the investigated concentration range (see Fig. 8*A*). This discrepancy with respect to the observed behavior (see Fig. 5*B*) appears intrinsic to the Scheme 1 and not dependent on the relative rate constants of the different steps; therefore, Scheme 1 does not seem sufficient for quantitatively describing the system behavior. From the phenomenological viewpoint, the system requires a fast unimolecular step that displaces the thermodynamic equilibrium in favor of the species characterizing the rate-limiting process, rendering the amount and the rate constant for the formation of the final product (*i.e.* Complex 3) independent of the concentration of the reactants F1 and F2. The most plausible event responsible for this behavior is a conformational change, although the structural features involved in this intermediate step are clearly arbitrary at this stage. Consequently, we have introduced a step 1A, leading to Complex 1A, which we have associated with a conformational change likely occurring immediately after the Complex 1 formation and leading to an unfavorable structural arrangement for the "His misligation". This new pathway is described in Scheme 2.

TABLE I
Kinetic parameters employed for simulation according to Schemes 1 and 2 and reported in Fig. 8, A and B

	Scheme 1	Scheme 2
k_{+1} (M^{-1} s^{-1})	7.2×10^6	7.2×10^6
k_{-1} (s^{-1})	21.9	21.9
k_{+1A} (s^{-1})		500
k_{-1A} (s^{-1})		0.1
k_{+2} (s^{-1})	0.11	0.11
k_{-2} (s^{-1})	0.01	0.01
k_{+3} (s^{-1})	200	200
k_{-3} (s^{-1})	0.01	0.01

This variation renders the kinetics of the formation of Complex 3 independent of the concentration of F1 (see Fig. 8*B*) as indeed it is observed in the experiments (see Fig. 5*B*). The applicability of this scheme is also supported by kinetic observations following CD changes (Fig. 9). Thus, at pH 7.0, where the formation of the Fe-Met bond is followed at 416 nm (see Fig. 3*C*), we observed a very slow process (Fig. 9*A*), characterized by a rate constant closely similar to that measured by optical

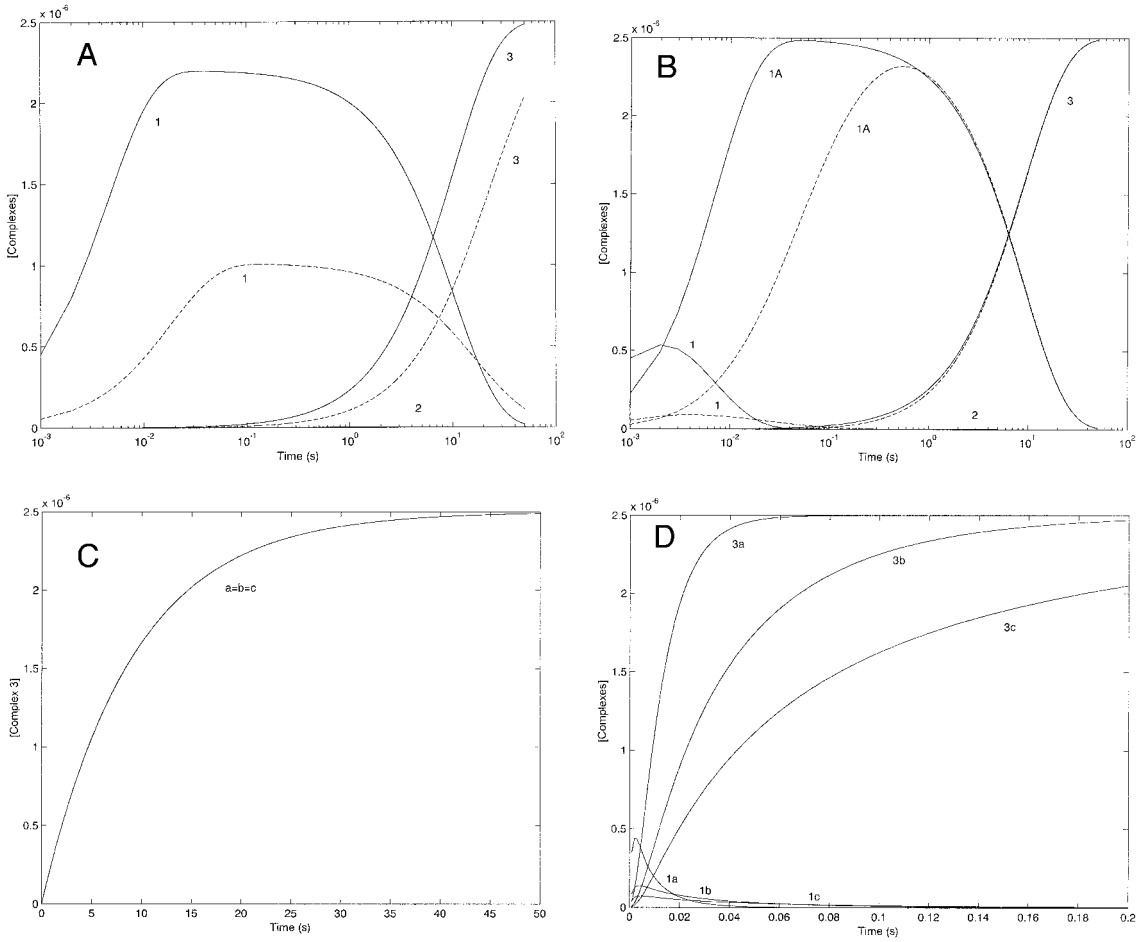

FIG. 8. **Kinetic simulation of complex formation.** *A*, simulation of time evolution for different intermediate forms (as indicated by *digits*) at pH 7.0 according to Scheme 1 and employing parameters reported in Table I, following the mixing of 2.5 μM F2 with 3.1 μM F1 (*thin dashed line*) or with 25 μM F1 (*thick continuous line*). *B*, simulation of time evolution for different intermediate forms (as indicated by *digits*) at pH 7.0 according to Scheme 2 and employing parameters reported in Table I, following the mixing of 2.5 μM F2 with 3.1 μM F1 (*thin dashed line*) or with 25 μM F1 (*thick continuous line*). *C*, simulation of time evolution at pH 7.0 of Complex 3 at different values of rate constants for the formation of Complex 1A (*i.e.* k_{+1A}, see Scheme 2) and for the formation of Complex 3 (*i.e.* k_{+3}, see Scheme 2). [F1] = 25 μM and [F2] = 2.5 μM, using the same parameters as above, except for k_{+1A} (100 s^{-1} in *curve a* and 500 s^{-1} in *curves b* and *c*) and for k_{+3} (10 s^{-1} in *curves a* and *b*, and 200 s^{-1} in *curve c*). It must be noted that *curves a–c* are overlapping. *D*, simulation of time evolution at pH 3.8 for Complex 1 and Complex 3 formation after the mixing of 2.5 μM F2 with 3.1 μM F1 (*curve a*), 6.2 μM F1 (*curve b*), and 25 μM F1 (*curve c*). The following parameters have been employed: $k_{+1} = 5.6 \times 10^6$ M^{-1} s^{-1}, $k_{-1} = 3.5$ s^{-1}, $k_{+1A} = 500$ s^{-1}, $k_{-1A} = 0.1$ s^{-1}, $k_{+3} = 200$ s^{-1}, $k_{-3} = 0.01$ s^{-1}. For further details, see text.

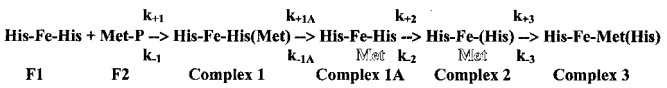

SCHEME 2

absorption at 408 and 695 nm (see Fig. 5*A*). On the other hand, at 225 nm, where the formation of the α-helical structure is followed by the complex assembly of the fragments (see Fig. 2), we detected a much faster process (Fig. 9*B*), which is characterized by a rate constant linearly dependent upon the concentration of the F1 fragments (see Fig. 9*C*) and by a second-order bimolecular rate constant (k) closely similar to that expected for the bimolecular process of complex formation (see Figs. 6 and 9*C*). In addition, the amplitude of the signal in millidegrees corresponds closely to that expected for the formation of $\approx$0.5 μM complex with a 0.1-cm path length (see Fig. 2). It clearly indicates that the structural transition, following the fragment complex formation and leading to complex 1A (see Scheme 2), is very fast, and it is rate-limited by the two fragments assembly. Therefore, according to this new scheme the assembly kinetics of the two fragments turn out to be characterized by a bimolecular process in which F1 and F2 react to form Complex 1, which rapidly converts to Complex 1A (see Table I), possibly characterized by a structural change of the relative positions of Met-80 and of the misligated His. Such a conformational change (underlined by the different character employed for Met in Scheme 2) renders thermodynamically (and kinetically) a more favorable evolution toward Complex 2, which is rate-limited by the His detachment, and it is then followed by a rapid binding of Met-80 to the (now free) sixth coordination position of the heme-iron (see Table I). It must be outlined that according to Scheme 2, the observed rate of formation of Complex 3 (corresponding to our measurements at 408 and 695 nm) appears now independent of the intrinsic rate constants for formation of Complex 1A (*i.e.* k_{+1A}, Fig. 8*C*, *curves a* and *b*) and Complex 3 (*i.e.* k_{+3}, Fig. 8*C*, *curves b* and *c*), clearly indicating that indeed dissociation of the misligated His must be the main determinant in the process.

Kinetics performed at lower pH values show a dependence of the rate constant on F1 concentration both at 280 and 408 nm (see Figs. 6 and 7) indicating that the formation of Complex 1A is probably very similar. However, under these conditions it evolves quickly toward Complex 3, because the rate-limiting event (corresponding to the formation of Complex 2) does not take place. The misligated His is protonated at pH 3.8, and it is not able to coordinate the heme iron anymore (even in F1, as

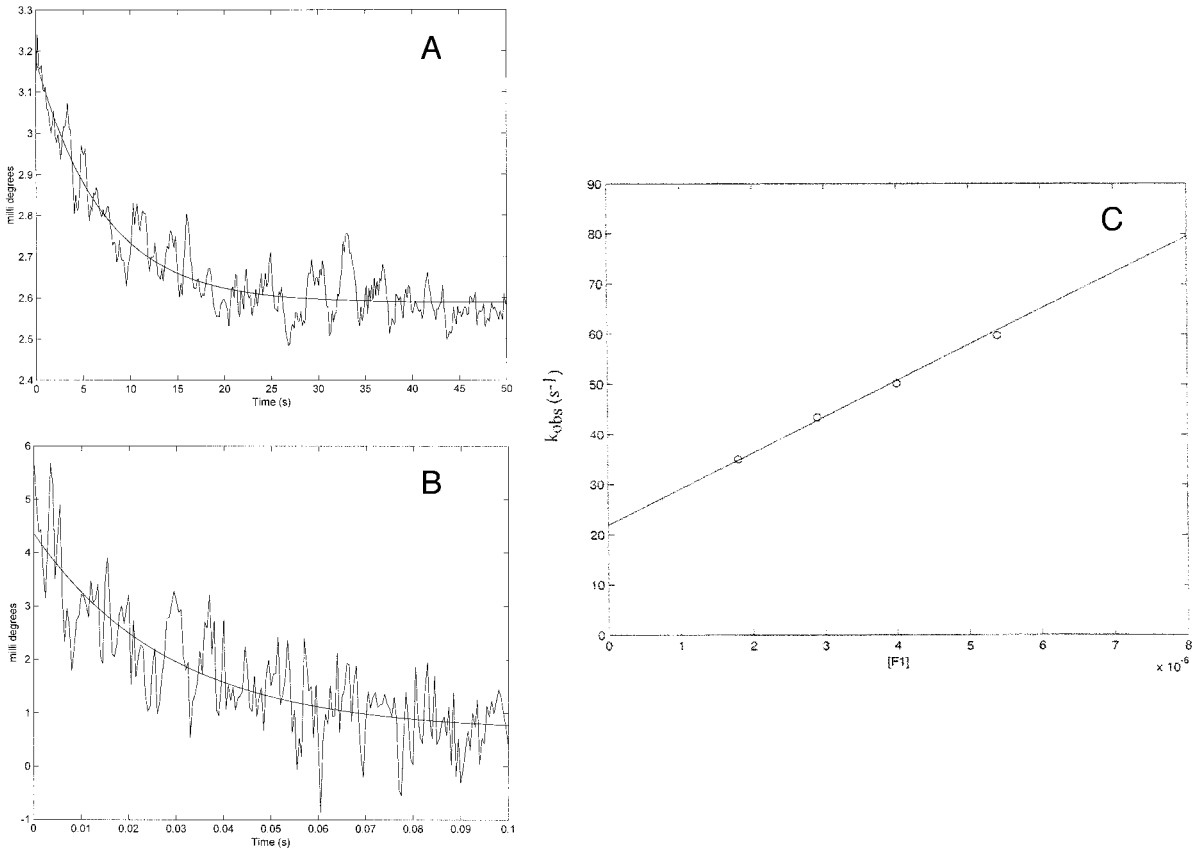

FIG. 9. **Circular dichroism kinetics.** *A*, circular dichroism signal at 416 nm, following the mixing of 5 μM F1 and 5 μM F2 fragment at pH 7.0 and 20 °C. The *signal* is the average of 12 measurements, and the *continuous line* is the least-squares fitting of data according to the equation in the legend to Fig. 5 with the following parameters: $S_\infty = 2.59 \pm 0.31$, $\Delta S = 0.59 \pm 0.07$, $k = 0.144 \pm 0.017$. *B*, circular dichroism signal at 225 nm, following the mixing of 4 μM of F1 and of 1.0 μM of F2 fragments at pH 7.0 and 20 °C (to a final complex concentration of 0.5 μM). The *signal* is the average of 19 measurements, and the *continuous line* is the least-squares fitting of data according to the equation in the legend to Fig. 5 with the following parameters: $S_\infty = 0.67 \pm 0.08$, $\Delta S = -3.69 \pm 0.47$, $k = 35.05 \pm 3.87$. *C*, dependence of k_{obs} at 225 nm on F1 concentration. For all experiments the concentration of F2 was 0.5 μM after mixing. The *continuous curve* is the least-squares fitting of data according to the equation in the legend to Fig. 6, with the following parameters: $k_{on} = 7.23 \pm 0.81 \times 10^6$ M^{-1} s^{-1}, $k_{off} = 21.9 \pm 2.8$ s^{-1}. For further details, see text.

indicated by the spectral change, see Fig. 3*A*), thus rendering much more similar the observations at the different wavelengths. However, it must be outlined that the second-order rate constant calculated at 280 nm ($5.6 (\pm 0.6) \times 10^6$ M^{-1} s^{-1}) is faster than that at 408 nm ($3.5 (\pm 0.4) \times 10^6$ M^{-1} s^{-1}). This observation can be accounted for by considering that formation of Complex 3 is somewhat slower than that of Complex 1 even in the absence of the rate-limiting step (corresponding to the formation of Complex 2, see Fig. 8*D*). In this respect, it may be interesting to outline that the simulation for the formation of Complex 3 as a function of concentration of F1 shows a pathway (see Fig. 8*D*) that closely corresponds to that observed from progress curves (see Fig. 7) and it requires a rate-limiting step with $k \cong 200$ s^{-1}. According to the simulation, this can be independently ascribed to the formation of either Complex 1A or Complex 3 and cannot be attributed unequivocally at this stage.

As a whole, the process of the recombination of the fragments into the complex can be described through two main steps. In the first step, Complex 1 is formed and rapidly evolves toward Complex 1A; at this stage, the rate-limiting step is the bimolecular formation of Complex 1 (see Scheme 2), as also demonstrated by kinetic CD data (see Fig. 9*B*). In the second step, over the pH range between 4.0 and 7.0, dissociation of the misligated His takes place, being the rate-limiting step of the overall process, followed by a rapid coordination of Met-80 to the heme-Fe(III), with formation of Complex 3. Because variations of the rate constant for formation of Complex 1A do not affect that for Complex 3 (the same is true for the rate constant of Complex 3 formation from Complex 2, see Fig. 8*C*), we can identify the Complex 1 → Complex 1A transition as the process responsible for the formation of the α-helical secondary structure following the initial collapse of the random coil fragments (17), as described previously for the early folding of cyt *c* (21–23). This process facilitates the formation in the complex of a tertiary structure that renders thermodynamically (and kinetically) more favorable the replacement of the misligated His by the native axial ligand Met-80. From a kinetic standpoint, this process takes place at a rate slower than that reported for native cyt *c* (10), thus suggesting that the conformation of the fragment complex renders less favorable the replacement of the misligated His. On the other hand, the observations at pH 3.8 indicate that in the absence of misligation the process is much faster, and it is rate-limited by the binding rate of Met-80 to the heme-Fe(III).

In conclusion, from these data emerges the importance for the folding process of the transmission of structural information among different domains of the same molecule. The interaction energy between them during the folding process represents the driving force, which pushes the structure toward the correct arrangement. Thus, the alteration of this communication pathway, as it occurs in the complex of the two fragments with respect to the native cyt *c*, brings about structural arrangements, which are somewhat unfavorable for the correct folding, probably requiring additional conformational changes that enhance the activation energy barriers for the process.

Acknowledgments—We thank Prof. G. Smulevich and Prof. C. Viappiani for several stimulating discussions.

REFERENCES

1. Dill, K. A., and Chan, H. S. (1997) *Nat. Struct. Biol.* **4,** 10–19
2. Jones, C. M., Henry. E. R., Hu, Y., Chan, C.-K., Luck, S. D., Bhuyan, A., Roder, H., Hofrichter, J., and Eaton, W. A. (1993) *Proc. Natl. Acad. Sci. U. S. A.* **90,** 11860–11864
3. Eaton, W. A., Muñoz, V., Hagen, S. J., Jas, G. S., Lapidus, L. J., Henry, E. R., and Hofrichter, J. (2000) *Annu. Rev. Biophys. Biomol. Struct.* **29,** 327–359
4. Myers, J. K., and Oas, T. G. (2002) *Annu. Rev. Biochem.* **71,** 783–815
5. Moore, G. R., and Pettigrew, G. W. (1990) *Cytochromes c. Evolutionary, Structural and Physiological Aspects*, Berlin, Germany, Springer-Verlag.
6. Bushnell, G. W., Louie, G. V., and Brayer, G. D. (1990) *J. Mol. Biol.* **214,** 585–595
7. Pierce, M. M., and Nall, B. T. (2000) *J. Mol. Biol.* **298,** 955–969
8. Elöve, G. A., Bhuyan, A. K., and Roder, H. (1994) *Biochemistry* **33,** 6925–6935
9. Pierce, M. M., and Nall, B. T. (1997) *Protein Sci.* **6,** 618–627
10. Colòn, W., Wakem, L. P., Sherman, F., and Roder, H. (1997) *Biochemistry* **36,** 12535–12541
11. Yeh, S.-R., and Rousseau, D. L. (1999) *J. Biol. Chem.* **274,** 17853–17859
12. Bai, Y. (1999) *Proc. Natl. Acad. Sci. U. S. A.* **96,** 477–480
13. Yeh, S.-R., Takahashi, S., Fan, B., and Rousseau, D. L. (1997) *Nat. Struct. Biol.* **4,** 51–56
14. Yeh, S.-R., and Rousseau, D. L. (1998) *Nat. Struct. Biol.* **5,** 222–228
15. Fontana, A., Zambonin, M., De Filippis, V., Bosco, M., and Polverino de Laureto, P. (1995) *FEBS Lett.* **362,** 266–270
16. Santucci, R., Fiorucci, L., Sinibaldi, F., Polizio, F., Desideri, A., and Ascoli, F. (2000) *Arch. Biochem. Biophys.* **379,** 331–336
17. Sinibaldi, F., Fiorucci, L., Mei, G., Ferri, T., Desideri, A., Ascoli, F., and Santucci, R. (2001) *Eur. J. Biochem.* **268,** 4537–4543
18. Pielak, G. J., Oikawa, K., Mauk, A. G., Smith, M., and Kay, C. M. (1986) *J. Am. Chem. Soc.* **108,** 2724–2727
19. Sosnick, T. R., Mayne, L., Hiller, R., and Englander, S. W. (1994) *Nat. Struct. Biol.* **1,** 149–156
20. Stellwagen, E., and Cass, R. (1974) *Biochem. Biophys. Res. Comm.* **60,** 371–375
21. Hagen, S. J., Hofrichter, J., Szabo, A., and Eaton, W. A. (1996) *Proc. Natl. Acad. Sci. U. S. A.* **93,** 11615–11617
22. Shastry, M. C. R., and Roder, H. (1998) *Nat. Struct. Biol.* **5,** 385–392
23. Akiyama, S., Takahashi, S., Ishimori, K., and Morishima, I. (2000) *Nat. Struct. Biol.* **7,** 514–520